Geotech Geol Eng
https://doi.org/10.1007/s10706-024-02917-y

ORIGINAL PAPER

Seismic Bearing Capacity of Shallow Foundations Under Large Earthquakes Using an Extended Pseudo-Dynamic Method

M. Mobini · M. Jiryaei Sharahi

Received: 28 December 2023 / Accepted: 8 August 2024

Abstract The seismic bearing capacity of foundations is an essential issue in seismically active regions, especially during significant earthquakes. This study presents an innovative time-domain pseudo-dynamic approach for estimating the seismic bearing capacity of strip foundations. By incorporating time-history ground motion, the analysis utilizes a composite failure surface that integrates active, logarithmic spiral, and passive zones to effectively capture the seismic response. Applying this method to significant earthquakes requires considering post-peak reduction in shear strength and shear wave velocity of the soil deposit. Furthermore, a comparative analysis is conducted, comparing the results with select experimental and analytical results from the literature. To explore further, a parametric study assesses the impact of key parameters, including shear wave velocity, soil layer thickness, frequency content, depth embedment, foundation width, damping ratio, shear strength parameters, and peak ground acceleration. The results indicate a more rapid decline in bearing capacity compared to previous studies.

Keywords Large earthquake · Bearing capacity · Foundation · Extended pseudo-dynamic

M. Mobini · M. J. Sharahi (✉)
Civil Engineering Department, Qom University of Technology, Qom, Iran
e-mail: jiryaei@qut.ac.ir

1 Introduction

Estimating the seismic bearing capacity of shallow foundations is a critical issue in earthquake-prone regions. Observations from significant earthquakes such as the one that occurred on February 6, 2023, in Turkey indicated that structures constructed by the same contractor displayed varying levels of resilience, with some remaining intact while others suffered damage (Franke et al. 2019; Maleki et al. 2019, 2023). One of the primary factors contributing to this discrepancy is the variability in the reduction of the seismic bearing capacity of shallow foundations. In large earthquakes where soil behavior becomes nonlinear, the seismic bearing capacity of shallow foundations presents a complex challenge influenced by various factors. Therefore, further research is essential to investigate different aspects of this issue.

Seismic accelerations are well-known for exerting inertial forces on both the structure and the underlying soil mass, thereby diminishing the seismic bearing capacity of foundations. Despite the detailed recording of seismic acceleration time histories using accelerometers, these records have not been applied in analytical methods for evaluating the seismic bearing capacity of foundations. In most previous studies, a constant acceleration or a harmonic acceleration with a fixed frequency was used instead of recorded earthquake acceleration time histories. Therefore, the interaction of frequencies was neglected.

Published online: 17 September 2024

Traditionally, analytical methods have primarily relied on the pseudo-static approach, characterized by constant accelerations. Several techniques have been employed within the pseudo-static approach framework to evaluate the seismic bearing capacity of foundations. These techniques include limit analysis (Conti 2018; Zhang et al. 2020; Mortara 2021), the stress characteristics method (Cascone et al. 2016; Ganesh et al. 2022; Casablancaet al. 2023), the limit equilibrium method (Nouzari et al. 2021), the finite element method (Nguyen et al. 2022; Jitchaijaroen et al. 2024; Garzón-Roca et al. 2024), and the finite difference method (Hamrouni et al. 2021). The pseudo-static approach is also commonly used for other aspects of geotechnical earthquake engineering, e.g., (Maleki et al. 2021, 2022; Rahmani et al. 2022). Additionally, Ghosh et al. (2017) and Debnath et al. (2018) evaluated the seismic bearing capacity of cohesive-frictional soil using this approach, considering concurrent resistance factors of unit weight, surcharge, and cohesion. Despite the widespread use of the pseudo-static approach due to its simplicity, it assumes seismic accelerations to be time-independent and constant with depth. As a result, it neglects dynamic factors such as wave propagation, amplification, phase difference, and ground motion frequency content.

The limitations of the pseudo-static approach led to the development of the pseudo-dynamic approach for the estimation of seismic earth pressure on retaining walls (Steedman et al. 1990; Choudhury et al. 2005; Debnath et al. 2018). The application of this approach has also been extended to seismic bearing capacity analysis (Choudhury et al. 2006; Ghosh et al. 2008; Saha et al. 2015; Izadi et al. 2021, 2022; Zhong et al. 2022; Chen et al. 2022). The pseudo-dynamic approach, despite its advantages, does not incorporate the zero-stress condition at the ground surface in its equations and requires an assumption regarding the amplification factor of the underlying soil deposit. Moreover, the pseudo-dynamic approach assumes a linear variation of the soil deposit amplification factor with depth.

Furthermore, Belleza (2014, 2015) introduced a modified pseudo-dynamic approach to address the limitations of the pseudo-dynamic approach and inherently consider the amplification factor. In a subsequent study, Zhou et al. (2023), (Krishnan and Chakraborty 2021), and Akhavan Tavakoli et al. (2023) incorporated this approach into finite element limit analysis procedures. Moreover, Saha et al. (2020), Debnath et al. (2021) and Nadgouda et al. (2023) applied this approach to determine the seismic bearing capacity of strip foundations using the limit equilibrium method. Kang et al. (2024) evaluated the seismic bearing capacity based on this approach, adopting the nonlinear Mohr–Coulomb criterion. The modified pseudo-dynamic approach, like the pseudo-dynamic approach, is designed to respond to harmonic excitation, while disregarding the recorded ground motion and its characteristics. Additionally, its further development is impeded by the elimination of the imaginary part of the equations and the emergence of hyperbolic functions. Notably, the existing literature lacks examination of the effects of ground motion frequency content and the predominant natural period of the soil deposit on seismic bearing capacity. Analytical techniques have also been developed without considering the effects of significant earthquakes on seismic bearing capacity.

The aim of this study, is to develop an extended pseudo-dynamic approach to estimate the seismic bearing capacity of strip foundations by considering the time-history seismic accelerations recorded during large earthquakes. This approach inherently accounts for the frequency content of the ground motion and its interactions with the natural periods of the soil deposit. Progressing incrementally in time enables the incorporation of nonlinear values based on stress–strain conditions, allowing for the consideration of shear strength reduction from peak to residual values and the decrease in shear wave velocity within the soil deposit (Seed et al. 1986). Therefore, the primary innovations of this study are: i) Considering the recorded earthquake acceleration as an input excitation in the time domain, none of the analytical methods previously presented have this capability. ii) The inclusion of non-linear behavior, which has been overlooked in previous analytical methods, leading to more realistic results.

In this study, the subgrade soil is assumed to be a frictional cohesive material with viscoelastic behavior. Since soil behavior exhibits nonlinearity during medium and large earthquakes, this study represents the seismic bearing capacity with a single coefficient denoted as $N_{\gamma e}$ for the three resistance components: unit weight, surcharge, and cohesion. The failure mechanism involves a composite planar and logarithmic spiral surface. The transient accelerations are computed for the active and passive triangular zones, along with the radial shear zone based on the wave propagation theory. This method considers the imaginary part of the response while implicitly considering the amplification of the soil deposit layer. The results of the proposed approach are consistent with some experimental and analytical results available in the literature. Considering a large earthquake a parametric study is conducted to evaluate the impacts of the ratio of soil deposit thickness to soil shear wave velocity, frequency content, soil damping ratio, and other influencing factors on the seismic bearing capacity of strip footings. The results of the parametric study indicate a more rapid decline in bearing capacity compared to previous findings, highlighting the significant challenge faced by shallow foundations in large earthquakes.

2 Method of Analysis

2.1 Problem Definition and Assumptions

To estimate the seismic bearing capacity of shallow foundations, a rupture mechanism is first considered. Once the failure mechanism is determined, the static forces can be easily calculated. In order to determine the inertial forces, it is necessary to use wave propagation equations to determine the average seismic acceleration in each zone. After determining the static and dynamic forces, the seismic bearing capacity can be calculated using equilibrium equations.

Figure 1 illustrates a strip foundation with a width of B, placed at a depth of D on dry viscoelastic frictional cohesive (φ–c) soil, where φ represents the soil friction angle and c is the soil cohesion. The failure mechanism for strip foundations is divided into three distinct zones: an active triangular zone beneath the footing labeled ABC, a transitional logarithmic spiral zone marked OCD, and a passive triangular zone denoted as ADE. During seismic events, the failure mechanism displays asymmetry, with one side (left side) being smaller than the other side (right side). The vertical distance from the center O to the ground surface, represented by d, can be easily determined as

$$d = \frac{r_0 sin\psi cos(\beta - \varphi + \alpha)}{cos(\theta - x - \alpha)} - D \quad (1)$$

where r_0 represents the initial radius of the log spiral zone, and θ is the angle between r_0 and OD, creating the log-spiral part. x indicates the angle of r_0 relative to the vertical. Angles α and β are the basic angles of the active triangular zone; while ψ and X represent the basic angles of the passive triangular zone as illustrated in Fig. 2

The highest stress gradient is observed at the edge of the foundation (point A). Therefore, as shown in Fig. 2, the assumption is made that the center of the logarithmic spiral (point O) aligns with the corner of the foundation (point A) (Budhu et al. 1993). Geometrically, this implies that with increased seismic acceleration, the angle β decreases proportionally to the increment in the angle α. The chosen composite

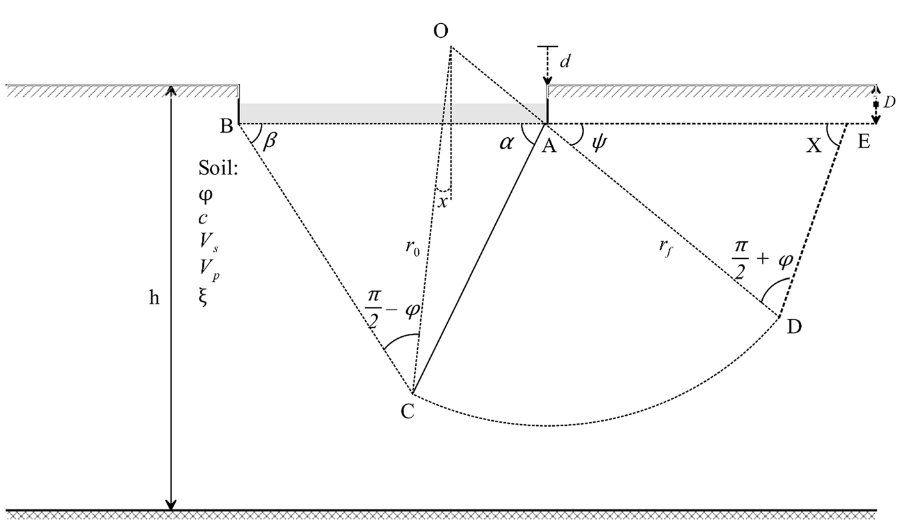

Fig. 1 General failure mechanism

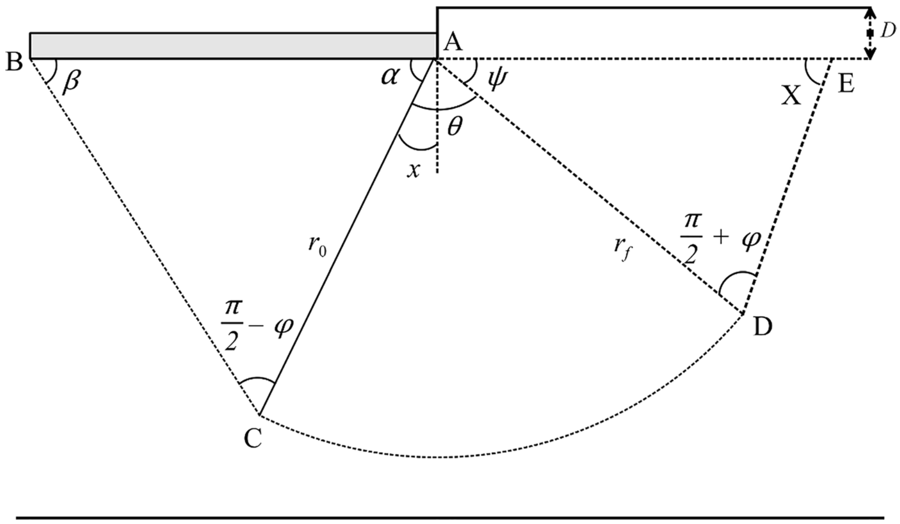

Fig. 2 General failure mechanism where the centre of the log spiral is located at A

failure surface is asymmetric as the angles α and β (or ψ and X) are not equal. Utilizing a search method with small increments in active angles (α or β) and passive angles (ψ or X) yields the most critical failure surface to obtain the minimum seismic bearing capacity. Note that in Fig. 1, when point O is located at point A, as shown in Fig. 2, the distance d must equal $-D$ and (β-$\varphi+\alpha$) must equal $\pi/2$.

In order to obtain the inertia forces and seismic acceleration of each zone, it is necessary to solve the wave propagation equations. The velocities of soil shear and primary waves, as well as the damping ratio, are denoted by V_s, V_p, and ξ, respectively. In accordance with the Kelvin-Voigt model for soil as a viscoelastic material, the equation of motion governing the vertical propagation of shear and primary waves through a homogeneous soil can be expressed as follows (Bellezza 2015):

$$\rho\frac{\partial^2 u_h}{\partial^2 t} = G\frac{\partial^2 u_h}{\partial^2 z} + \eta_s\frac{\partial^3 u_h}{\partial^2 z\partial t} \tag{2}$$

$$\rho\frac{\partial^2 u_v}{\partial^2 t} = (\lambda + 2G)\frac{\partial^2 u_v}{\partial^2 z} + (\eta_1 + 2\eta_s)\frac{\partial^3 u_v}{\partial^2 z\partial t} \tag{3}$$

where u_h and u_v are the horizontal and vertical components of the displacement, η_s and G represent the viscous damping and shear modulus of the soil, respectively; ρ, λ, and η_l indicate the density, the first Lame constant, and the viscosity component, respectively; t and z represent time and depth from the ground surface, respectively. γ and τ represent the shear strain and the shear stress, respectively, while ω denotes the angular frequency.

Solving Eqs. (2) and (3) yields the following transfer functions at a depth z beneath the ground surface for the soil layer above the solid bedrock (Jiryaei 2022):

$$f_{ha}(z,\omega) = \frac{\cos k_s^* z}{\cos k_s^* h} \tag{4}$$

$$f_{va}(z,\omega) = \frac{\cos k_p^* z}{\cos k_p^* h} \tag{5}$$

where f_{ha} and f_{va} are the horizontal and vertical components of the transfer functions, h represents the thickness of the soil deposit, and $k_p{}^*$ and $k_s{}^*$ denote the complex wave numbers corresponding to the P-wave and the S-wave, respectively.

By considering the horizontal and vertical components of seismic acceleration A_h and A_v in the Fourier domain, the acceleration components a_h and a_v at depth z can be calculated as (Jiryaei 2022)

$$a_h(z,\omega) = A_h\frac{\cos k_s^* z}{\cos k_s^* h} \tag{6}$$

$$a_v(z,\omega) = A_v\frac{\cos k_p^* z}{\cos k_p^* h} \tag{7}$$

Any random motion, such as seismic ground motion, can be defined as input to A_v and A_h. It is important to note that the modified pseudo-dynamic approach solely accounts for harmonic motion. Eqations. (6) and (7) are used to calculate the inertial forces acting on the soil mass below the footing.

2.2 Computations for Seismic and Static Forces

Once the failure mechanism is identified, the calculation of inertial forces exerted on the soil mass within a particular zone can be accomplished by utilizing the seismic accelerations outlined in Eqs. (6) and (7). In Figure 2, calculations can commence from the triangular passive zone ADE. To ascertain the passive resistance (P_{p1}) acting on GD between GDE and GDCA (as shown in Fig. 3), a hypothetical wall (GD) with a friction angle δ is assumed. P_{p1} is resolved into two components: P_{p1cq} represents the cohesion and surcharge component, while $P_{p1\gamma}$ denotes the unit weight component. These components are delineated separately because of variations in their application points. The friction angle δ in Fig. 3 is calculated as $\delta = C_d \times \varphi$, where C_d is a coefficient that ranges from -1 to $+1$ and depends on B, D, φ, and c; thus, C_d can be determined under static conditions. In Fig. 3, the sole unknown factor is P_{p1}, which is calculated by considering the equilibrium of horizontal and vertical forces acting on the GED:

$$P_{p1} = P_{p1cq} + P_{p1\gamma} \tag{8}$$

where

$$P_{p1cq} = \frac{1}{sin(\delta)tan(\varphi + X) - cos(\delta)}\Big[-2ch_2 tan(\varphi + X) - qh_2 cot(X)\left(1 - \frac{a_{vd}}{g}\right)tan(\varphi + X) - ch_2 cot(X) + qh_2 cot(X)\left(\frac{a_{hd}}{g}\right)\Big] \tag{9}$$

$$P_{p1\gamma} = \frac{1}{sin(\delta)tan(\varphi + X) - cos(\delta)}\left[Q_{v1} tan(\varphi + X) - W_1 tan(\varphi + X) + Q_{h1}\right] \tag{10}$$

q represents the surcharge, while h_2 indicates the depth of DGE:

$$h_2 = B\frac{sin(\psi)e^{\theta tan\varphi}}{cos(x)(cot(\alpha) + cot(\beta))} \tag{11}$$

W_1 is the weight of the GED:

$$W_1 = \gamma\frac{{h_2}^2}{2}cot(X) \tag{12}$$

Additionally, a_{hd} and a_{vd} in Eq. (9) represent seismic acceleration components at a depth of D:

$$a_{hd}(t) = ift\left(A_h\frac{\cos k_s^* D}{\cos k_s^* h}\right) \tag{13}$$

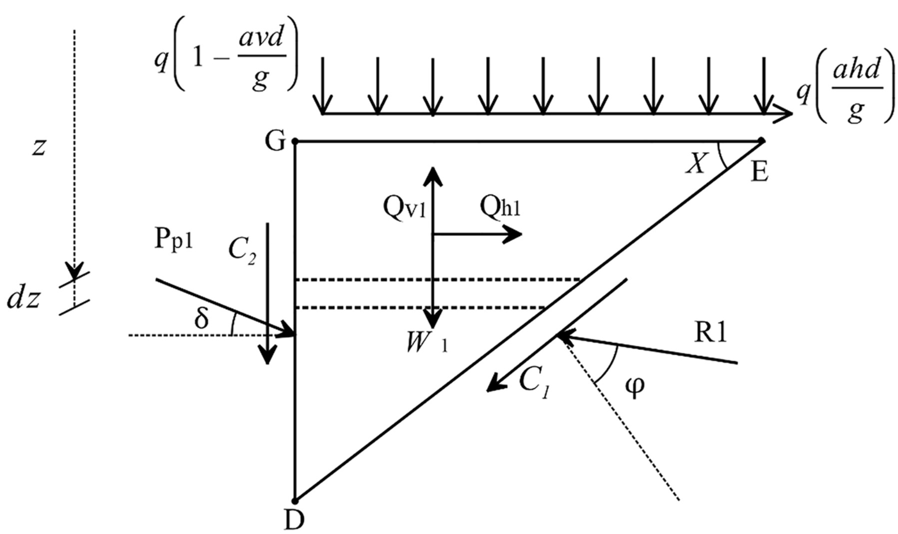

Fig. 3 The hypothetical wall GD with the frictional angle of δ

$$a_{vd}(t) = ift\left(A_v \frac{\cos k_p^* D}{\cos k_p^* h}\right) \quad (14)$$

where *ift* stands for the inverse Fourier transform.

Q_{h1} and Q_{v1} in Eq. (10) represent inertial forces acting on the GED due to the seismic accelerations. These inertial forces are calculated by integrating the product of a mass element and the seismic acceleration corresponding to the depth of the mass element. Therefore, amplification resulting from wave propagation is inherently taken into account. The calculation of dQ_{h1} for a small mass element dm is given by $dQ_{h1} = a_h \times dm$. thus,

$$Q_{h1}(t) = ift\left(\int a_h(z,\omega)dm\right) = ift\left\{\int_D^{h2+D}\left[\frac{A_h\cos\left(k_s z\right)}{\cos\left(k_s h\right)}\right]\left[\frac{\gamma}{g}\frac{\left(h_2 + D - z\right)}{\tan(X)}\right]dz\right\} = a_{ha1}(t)\frac{W_1}{g} \quad (15)$$

Similarly, in the vertical direction:

$$Q_{v1}(t) = ift\left(\int a_v(z,\omega)dm\right) = ift\left\{\int_D^{h2+D}\left[\frac{A_v\cos\left(k_p z\right)}{\cos\left(k_p h\right)}\right]\left[\frac{\gamma}{g}\frac{\left(h_2 + D - z\right)}{\tan(X)}\right]dz\right\} = a_{va1}(t)\frac{W_1}{g} \quad (16)$$

where

$$a_{ha1}(t) = ift\left\{\frac{2A_h}{k_s^2 h_2^2\cos\left(k_s h\right)}\left[-\cos\left(k_s h_2 + k_s D\right) - k_s h_2\sin\left(k_s D\right) + \cos\left(k_s D\right)\right]\right\} \quad (17)$$

$$a_{va1}(t) = ift\left\{\frac{2A_v}{k_p^2 h_2^2\cos\left(k_p h\right)}\left[-\cos\left(k_p h_2 + k_p D\right) - k_p h_2\sin\left(k_p D\right) + \cos\left(k_p D\right)\right]\right\} \quad (18)$$

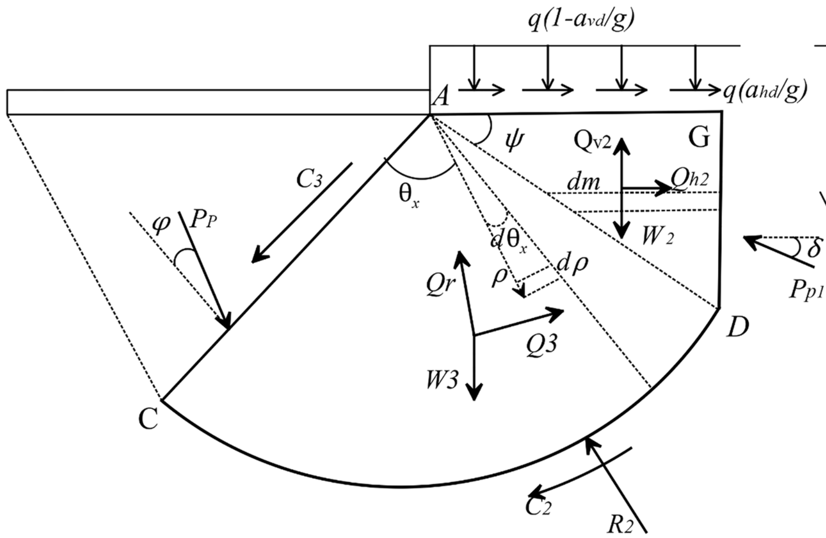

Fig. 4 Seismic and static forces acting on GDCA

a_{ha1} and a_{va1} represent the horizontal and vertical components of the weighted average acceleration for GED in the time domain. Multiplying these average accelerations by the mass of GED yields Q_{h1} and Q_{v1} in the time domain. Calculating the force $Pp1$ according to Eq. (8) helps determine the passive force of P_p on the GDCA. In Fig. 4, the force P_p can be determined by considering the equilibrium of moments around point A. It is important to note that the reaction force R_2 passes through the center of the logarithmic spiral and can be excluded from the moment equilibrium equation around point A.

$$P_p = \frac{M_{P1cqh} - M_{P1cqv} + M_q + M_{C2}}{\frac{1}{2} r_0 cos(\varphi)} + \frac{M_{P1\gamma h} - M_{P1\gamma v} + M_{W2} - M_{Qh2} - M_{Qv2} + M_{W3} - M_{Q3}}{\frac{2}{3} r_0 cos(\varphi)} \tag{19}$$

where M_{W2}, Mq, and Mc represent the moments of the weight of AGD (W_2) the surcharge (q), and the cohesive resistance along the logarithmic spiral (C_2), respectively. M_{P1cqh} and M_{P1cqv} denote the moments of components of $P1cq$ while $M_{P1\gamma h}$ and $M_{P1\gamma v}$ represent the moments of the components of $P1\gamma$.

$$M_{W2} = \int_D^{h2+D} \gamma \left(h_2 + D - z\right) cot\psi \left[h_2 cot\psi - \frac{\left(h_2 + D - z\right) cot\psi}{2} \right] dz = \frac{1}{3} \gamma cot^2(\psi) h_2^3 \tag{20}$$

$$M_q = q\left(1 - \frac{a_{vd}}{g}\right) h_2 cot(\psi) \left[\frac{h_2 cot(\psi)}{2}\right] \tag{21}$$

$$M_{P1cqh} = P_{p1cq} cos(\delta) \left[\frac{1}{2} h_2\right] \tag{22}$$

$$M_{P1\gamma h} = P_{p1\gamma} cos(\delta) \left[\frac{2}{3} h_2\right] \tag{23}$$

$$M_{P1cqv} = P_{p1cq} sin(\delta) \left[h_2 cot(\psi)\right] \tag{24}$$

$$M_{P1\gamma v} = P_{p1\gamma} sin(\delta) \left[h_2 cot(\psi)\right] \tag{25}$$

$$M_{C2} = \int_0^{\theta} c \frac{r}{\cos(\varphi)} [r\cos(\varphi)] d\theta_x = \frac{c{r_0}^2}{2tan(\varphi)} \left(e^{2\theta tan(\varphi)} - 1\right) \tag{26}$$

where θ_x represents the angle between the passing radius of any differential element and the initial radius as illustrated in Fig. 4.

By considering a differential element with infinitesimal thickness dz as shown in Fig. 4, the moment of the horizontal and vertical components of the inertial forces M_{Qh2} and M_{Qv2} about point A can be determined. It should be mentioned that the arm of each moment is simply determined using geometry, which is included within the brackets in the Eqs. (20)–(28), (31) and (33).

$$M_{Qh2} = ift\left\{ \int_D^{h_2+D} \frac{A_h cos\left(k_s z\right)}{cos\left(k_s h\right)} \frac{\gamma}{g} \left(h_2 + D - z\right) cot\psi [z - D] dz \right\} = a_{ha2}(t) \frac{M_{W2}}{g} \tag{27}$$

$$M_{Qv2} = ift\left\{ \int_D^{D+h2} A_v \frac{cos\left(k_p z\right)}{cos\left(k_p h\right)} \frac{\gamma}{g} \left(h_2 + D - z\right) cot\psi \left[h_2 cot\psi - \frac{\left(h_2 + D - z\right) cot\psi}{2} \right] dz \right\} = a_{va2}(t) \frac{M_{W2}}{g} \tag{28}$$

where,

$$a_{ha2}(t) = ift\left\{ \frac{3}{cot\psi k_s^3 h_2^3} \frac{A_h}{cos\left(k_s h\right)} \left[2sin\left(k_s h_2 + k_s D\right) - 2sin\left(k_s D\right) - k_s h_2 cos\left(k_s h_2 + k_s D\right) - k_s h_2 cos\left(k_s D\right)\right] \right\} \quad (29)$$

$$a_{va2}(t) = ift\left\{ \frac{3}{2h_2^3 k_p^3} \frac{A_v}{cos\left(k_p h\right)} \left[2sin\left(k_p h_2 + k_p D\right) - 2sin\left(k_p D\right) - 2k_p h_2 cos\left(k_p h_2 + k_p D\right) - h_2^2 k_p^2 sin\left(k_p D\right)\right] \right\} \quad (30)$$

a_{ha2} and a_{va2} represent the horizontal and vertical components of the weighted average acceleration for GAD in the time domain. The ADC weight moment M_{W3} and the inertial force moment M_{Q3} about point A can be computed by considering an element with dimensions $d\rho \times \rho d\theta_x$ as illustrated in Fig. 4, where ρ denotes the distance of this element from point A. It is noteworthy that M_{Qr} is zero and is hence eliminated from the moment equilibrium equation.

$$\begin{aligned} M_{W3} &= \gamma \int_0^\theta \int_0^r \rho\left[\rho \sin\left(\theta_x - x\right)\right] d\rho d\theta_x = \gamma \int_0^\theta \frac{r^3}{3} \sin\left(\theta_x - x\right) d\theta_x \\ &= \frac{\gamma r_0^3}{3\left(9tan^2(\varphi) + 1\right)} \left[cos(x) + 3tan(\varphi)sin(x) - e^{3\theta tan(\varphi)}(cos(\theta - x) - 3tan(\varphi)sin(\theta - x))\right] \end{aligned} \quad (31)$$

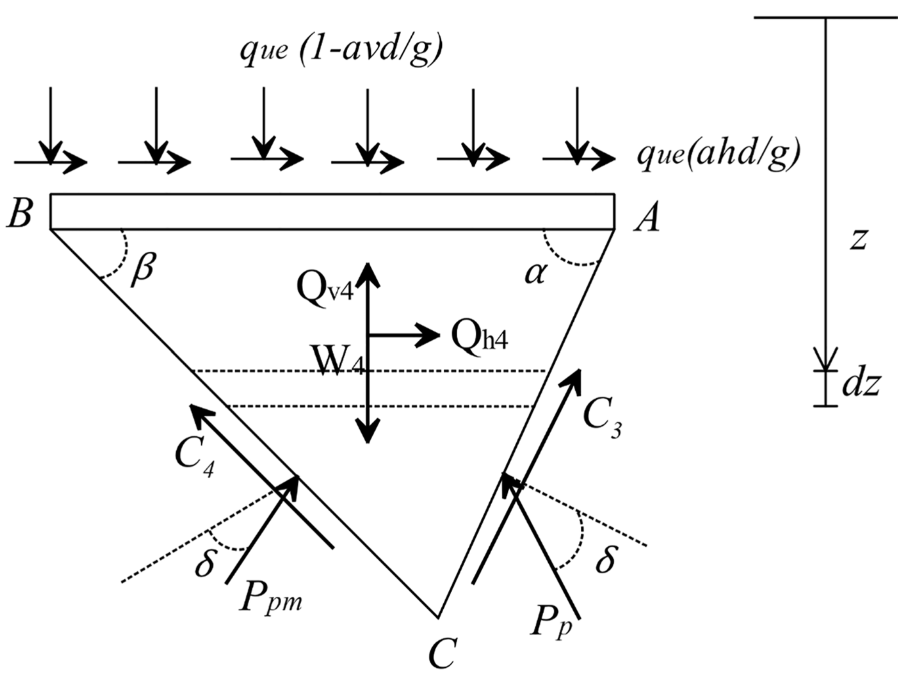

Fig. 5 Seismic and static forces acting on ABC

In polar coordinates with point A as the center, the seismic acceleration in the θ_x-direction a_θ can be calculated accordingly.

$$\begin{aligned} a_\theta =& a_h cos\left(\theta_x - x\right) + a_v sin\left(\theta_x - x\right) = A_h \frac{cos\left(k_s z\right)}{cos\left(k_s h\right)} cos\left(\theta_x - x\right) + A_v \frac{cos\left(k_s z\right)}{cos\left(k_p h\right)} sin\left(\theta_x - x\right) \\ &= A_h \frac{cos\left[k_s \rho cos\left(\theta_x - x\right) + k_s D\right]}{cos\left(k_s h\right)} cos\left(\theta_x - x\right) + A_v \frac{cos\left[k_p \rho cos\left(\theta_x - x\right) + k_p D\right]}{cos\left(k_p h\right)} sin\left(\theta_x - x\right) \end{aligned} \tag{32}$$

therefore,

$$\begin{aligned} M_{Q3} =& ift\left\{ \int_0^\theta \int_0^{r_0 \times exp\left(\theta_x tan(\varphi)\right)} A_h \frac{cos\left(k_s \rho cos\left(\theta_x - x\right) + k_s D\right)}{cos\left(k_s h\right)} \left[\rho cos\left(\theta_x - x\right)\right] \frac{\gamma}{g} \rho d\rho d\theta_x \right. \\ &\left. + \int_0^\theta \int_0^{r_0 \times exp\left(\theta_x tan(\varphi)\right)} A_v \frac{cos\left(k_p \rho cos\left(\theta_x - x\right) + k_p D\right)}{cos\left(k_p h\right)} \left[\rho sin\left(\theta_x - x\right)\right] \frac{\gamma}{g} \rho d\rho d\theta_x \right\} = \frac{\gamma}{g} \int_0^\theta cos\left(\theta_x - x\right) \\ &\times ift\left\{ \int_0^{r_0 \times exp\left(\theta_x tan(\varphi)\right)} A_h \frac{cos\left(k_s \rho cos\left(\theta_x - x\right) + k_s D\right)}{cos\left(k_s h\right)} \rho^2 d\rho \right\} d\theta_x + \frac{\gamma}{g} \int_0^\theta sin\left(\theta_x - x\right) \\ &\times ift\left\{ \int_0^{r_0 \times exp\left(\theta_x tan(\varphi)\right)} A_v \frac{cos\left(k_p \rho cos\left(\theta_x - x\right) + k_p D\right)}{cos\left(k_p h\right)} \rho^2 d\rho \right\} d\theta_x = \frac{\gamma}{g} \int_0^\theta cos\left(\theta_x - x\right) a_{ha3} \\ &\int_0^{r_0 \times exp\left(\theta_x tan(\varphi)\right)} \rho^2 d\rho d\theta_x + \frac{\gamma}{g} \int_0^\theta sin\left(\theta_x - x\right) a_{va3} \int_0^{r_0 \times exp\left(\theta_x tan(\varphi)\right)} \rho^2 d\rho d\theta_x = \frac{\gamma r_0^3}{3g} \int_0^\theta cos\left(\theta_x - x\right) a_{ha3} \\ &\exp\left((3\theta_x \tan((\varphi)))\right) d\theta_x + \frac{\gamma r_0^3}{3g} \int_0^\theta sin\left(\theta_x - x\right) a_{va3} \exp\left((3\theta_x \tan)(\varphi)\right) d\theta_x \end{aligned} \tag{33}$$

where,

$$\begin{aligned} a_{ha3}(t) =& ift\left\{ \frac{3A_h}{k_s^3 r_2^3 cos\left(k_s h\right) cos^3\left(\theta_x - x\right)} \left[2sin\left(k_s D\right) - 2sin\left(k_s r_2 cos\left(\theta_x - x\right)\right.\right.\right. \\ &\left. + k_s D\right) + 2k_s r_2 cos\left(\theta_x - x\right) cos\left(k_s r_2 cos\left(\theta_x - x\right) + k_s D\right) \\ &\left.\left. + k_s^2 r_2^2 cos^2\left(\theta_x - x\right) sin\left(k_s r_2 cos\left(\theta_x - x\right) + k_s D\right)\right]\right\} \end{aligned} \tag{34}$$

$$\begin{aligned} a_{va3}(t) =& ift\left\{ \frac{3A_v}{k_p^3 r_2^3 cos\left(k_p h\right) cos^3\left(\theta_x - x\right)} \left[2sin\left(k_p D\right) - 2sin\left(k_p r_2 cos\left(\theta_x - x\right) + k_p D\right)\right.\right. \\ &+ 2k_p r_2 cos\left(\theta_x - x\right) cos\left(k_p r_2 cos\left(\theta_x - x\right)\right. \\ &\left.\left.\left. + k_p D\right) + k_p^2 r_2^2 cos^2\left(\theta_x - x\right) sin\left(k_p r_2 cos\left(\theta_x - x\right) + k_p D\right)\right]\right\} \end{aligned} \tag{35}$$

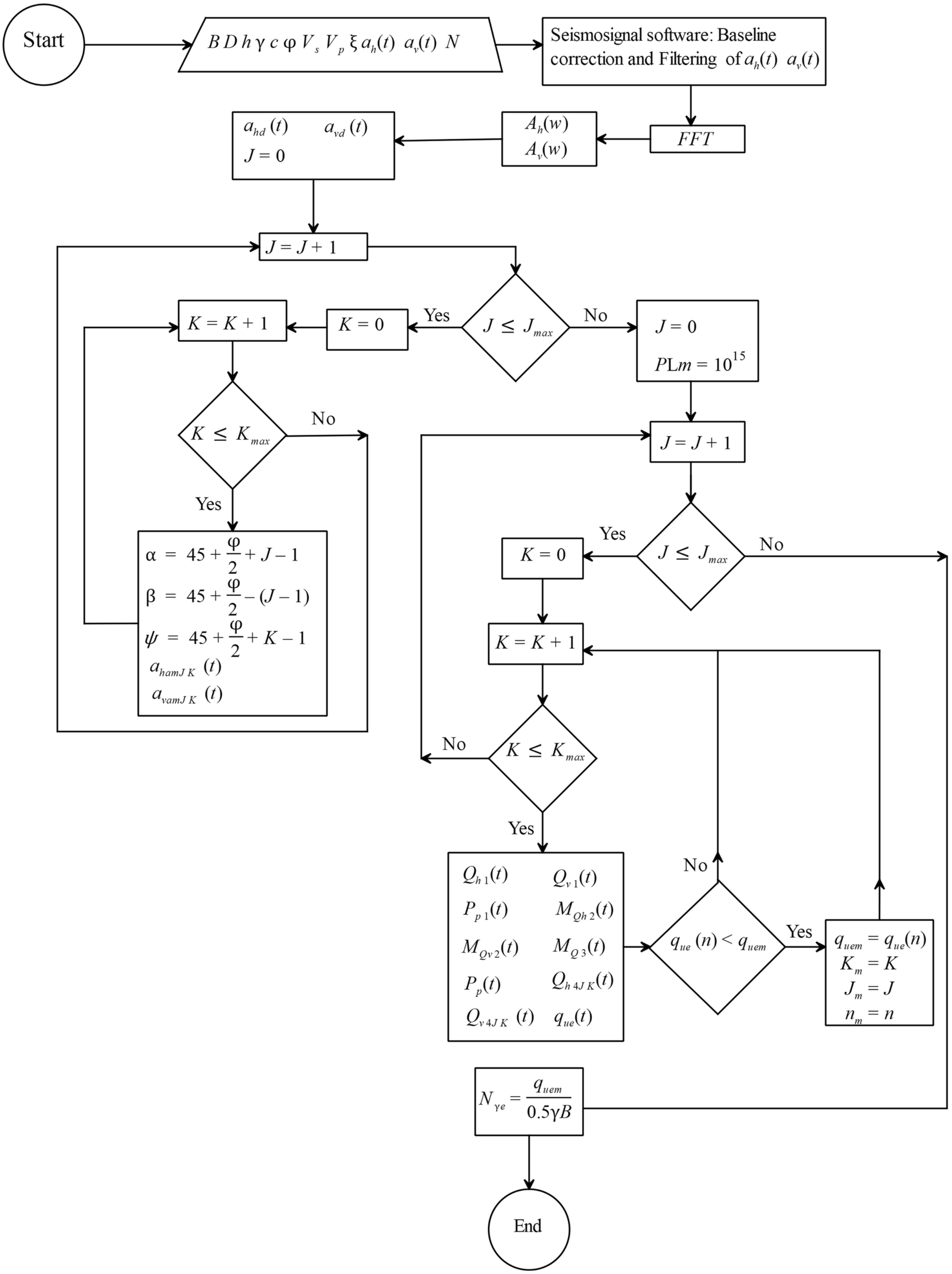
Start
B D h γ c φ V_s V_p ξ a_h(t) a_v(t) N
Seismosignal software: Baseline correction and Filtering of a_h(t) a_v(t)
FFT
A_h(w) A_v(w)
a_hd(t) a_vd(t) J = 0
J = J + 1
J ≤ J_max
Yes
No
K = 0
K = K + 1
K ≤ K_max
Yes
No
α = 45 + φ/2 + J − 1
β = 45 + φ/2 − (J − 1)
ψ = 45 + φ/2 + K − 1
a_hamJK(t)
a_vamJK(t)
J = 0
PLm = 10^15
J = J + 1
J ≤ J_max
Yes
No
K = 0
K = K + 1
K ≤ K_max
No
Yes
Q_h1(t) Q_v1(t) P_p1(t) M_Qh2(t) M_Qv2(t) M_Q3(t) P_p(t) Q_h4JK(t) Q_v4JK(t) q_ue(t)
q_ue(n) < q_uem
No
Yes
q_uem = q_ue(n)
K_m = K
J_m = J
n_m = n
N_γe = q_uem / 0.5γB
End

◂**Fig. 6** Flow chart of the program

$$r_2 = r_0 exp\left(\theta_x tan\varphi\right) \tag{36}$$

a_{ha3} and a_{va3} represent the horizontal and vertical components of the weighted average seismic acceleration for a sector of radius r_2 and angle $d\theta_x$ in the time domain where r_2 denotes the radius of the log-spiral at any θ_x. Consequently, M_{Q3} can be calculated through integration with respect to the single variable θ_x. The introduction of these average accelerations and the method for determining M_{W3} and M_{Q3} as described in Eqs. (31)–(36) for the radial shear zone of ADC can be viewed as additional innovations in this research.

2.3 Computations for Seismic Bearing Capacity

Figure 5 illustrates the forces acting on wedge ABC beneath the footing. P_{pm} and C_4 represent the cohesive and frictional resistance forces on the left side of the failure mechanism. It is assumed that full mobilization is achieved for cohesion, while partial mobilization is considered for the friction components. The calculation for C_4 is as follows:

$$C_4 = c\frac{h1}{sin\beta} \tag{37}$$

where h_1 represents the heigh of ABC triangle passing through point C. The only remaining unknowns are the seismic bearing capacity q_{ue} and P_{pm}. By applying the horizontal and vertical equilibrium equations to the forces acting on wedge ABC, these two variables can be determined. Therefore, q_{ue} and the seismic bearing capacity factor $N_{\gamma e}$ can be obtained as:

$$\begin{aligned} q_{ue} = & \frac{1}{B\left(1-\frac{a_{vd}}{g}\right)sin(\beta-\varphi)+B\left(\frac{a_{hd}}{g}\right)cos(\beta-\varphi)}\left[2ch_1 sin(\beta-\varphi)\right. \\ & +P_p cos(\alpha-\varphi)sin(\beta-\varphi)+Q_{v4}sin(\beta-\varphi)-W_4 sin(\beta-\varphi)-ch_1 cot(\alpha)cos(\beta-\varphi) \\ & \left.+P_p sin(\alpha-\varphi)cos(\beta-\varphi)+ch_1 cot(\beta)cos(\beta-\varphi)-Q_{h4}cos(\beta-\varphi)\right] \end{aligned} \tag{38}$$

$$N_{\gamma e} = \frac{q_{ue}}{\frac{1}{2}\gamma B} \tag{39}$$

where W_4 denotes the weight of wedge ABC:

$$W_4 = \frac{\gamma B h_1}{2} \tag{40}$$

The inertial forces of wedge ABC, Q_{h4} and $Q_{v4,}$ are calculated in a similar manner to the seismic forces Q_{h1} and Q_{v1}.

$$Q_{h4}(t) = a_{ha4}(t)\frac{W_4}{g} \tag{41}$$

$$Q_{v4}(t) = a_{va4}(t)\frac{W_4}{g} \tag{42}$$

where

$$a_{ha4}(t) = ift\left\{\frac{2A_h}{k_s^2 h_1^2 cos\left(k_s h\right)}\left[-cos\left(k_s h_1 + k_s D\right) - h_1 k_s sin\left(k_s D\right) + cos\left(k_s D\right)\right]\right\} \tag{43}$$

Table 1 Comparison of the proposed method results and the values measured in the shaking table test

Method	Static	Accelerations			
		0.16 g	0.21 g	0.26 g	0.31 g
Proposed method	10	8.11	7.98	7.86	7.74
Shaking table test (Knappett et al. 2006)	10	8.42	Failure	Failure	Failure

for wedge ABC in the time domain. Eq. (39) defines $N_{\gamma e}$ as an integrated seismic bearing capacity factor encompassing cohesion, surcharge, and unit weight resistance components. It is important to highlight that the non-linear behavior of the soil precludes the use of the principle of superposition. As a result, a seismic bearing capacity coefficient is applied to all components.

$$a_{va4}(t) = ift\left\{ \frac{2A_v}{k_p^2 h_1^2 cos\left(k_p h\right)} \left[-cos\left(k_p h_1 + k_p D\right) - h_1 k_p sin\left(k_p D\right) + cos\left(k_p D\right) \right] \right\} \tag{44}$$

a_{ha4} and a_{va4} represent the horizontal and vertical components of the weighted average acceleration

Table 2 Comparison of the proposed method results and the values measured in the shaking table test

	Critical acc. (g)	Input horizontal acceleration (g)	Bearing capacity (kN)	
			Measured	Proposed method
Model 1	0.08	$a_h = 0.064\ (t-2.5)\ \sin(6\pi t)$	615	607
Model 2	0.25	$a_h = 0.064\ (t-2.5)\ \sin(6\pi t)$	205	192

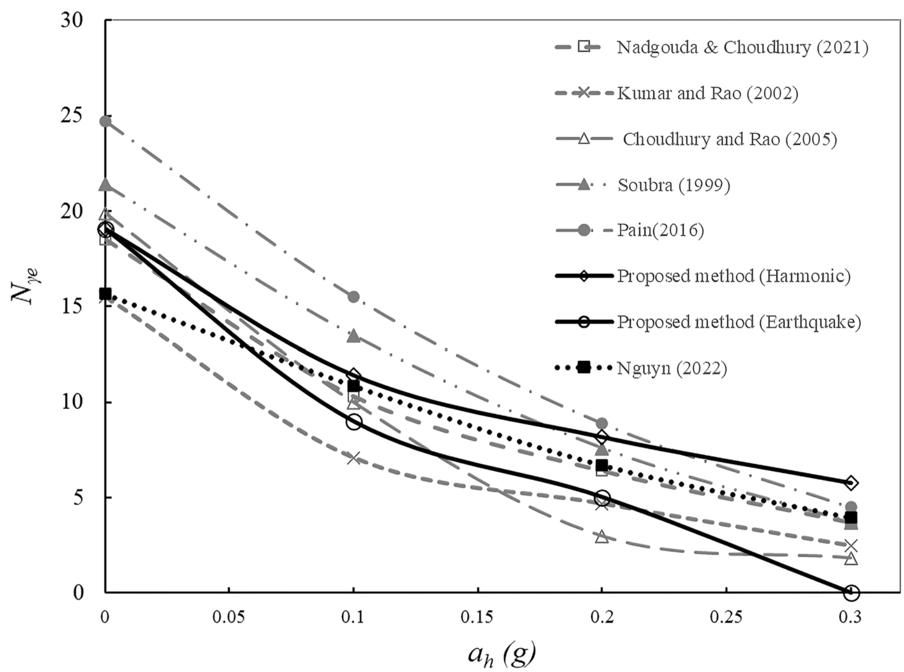

Fig. 7 Comparison of the results of the proposed method and the analytical results

3 Results and Discussion

The development of the extended pseudo-dynamic approach is the main achievement and innovation of this study. It can be used for estimating the seismic bearing capacity of shallow foundations. A computer program within the Matlab package has been developed to calculate the seismic bearing capacity of foundations according to the method proposed in this study. The program evaluates various values of the angles α, ψ, as well as the time step n treating them as independent geometric and temporal variables to estimate the minimum value of $N_{\gamma e}$. The input excitation is the random ground motion data recorded during an earthquake. Depending on the seismic activity in the specific area of interest, a seismic acceleration time history can be chosen from the earthquake database. Baseline correction and frequency filtering are typically conducted utilizing signal processing software like Seismsignal. Subsequently, the data is adjusted to achieve the desired peak ground acceleration denoted by *PGA*. Following building codes, this procedure is commonly carried out using an average of three or more previously recorded acceleration time histories from the specific target region. In order to derive A_h(w) and A_v(w), the scaled seismic acceleration is converted from the time domain to the Fourier domain. Additional parameters required for the program include D, B, c, φ, V_s, V_p, and ζ.

Figure 6 illustrates a flow chart detailing the program's operation. Within the flow chart: J and K serve as counters for seismic variations in α and ψ; n is the time step; q_{uem} represents the minimum of q_{ue}; J_m, K_m, and n_m correspond to the minimum of q_{uem}; m is an index assigned to $a_{ham}(t)$ where $m=1$, 2, 3, 4; *fft* represents the Fast Fourier Transform algorithm. The computations progress step by step in the time domain, enabling the consideration of alterations in soil shear and primary velocities, along with changes in cohesion and friction angle due to nonlinear behavior.

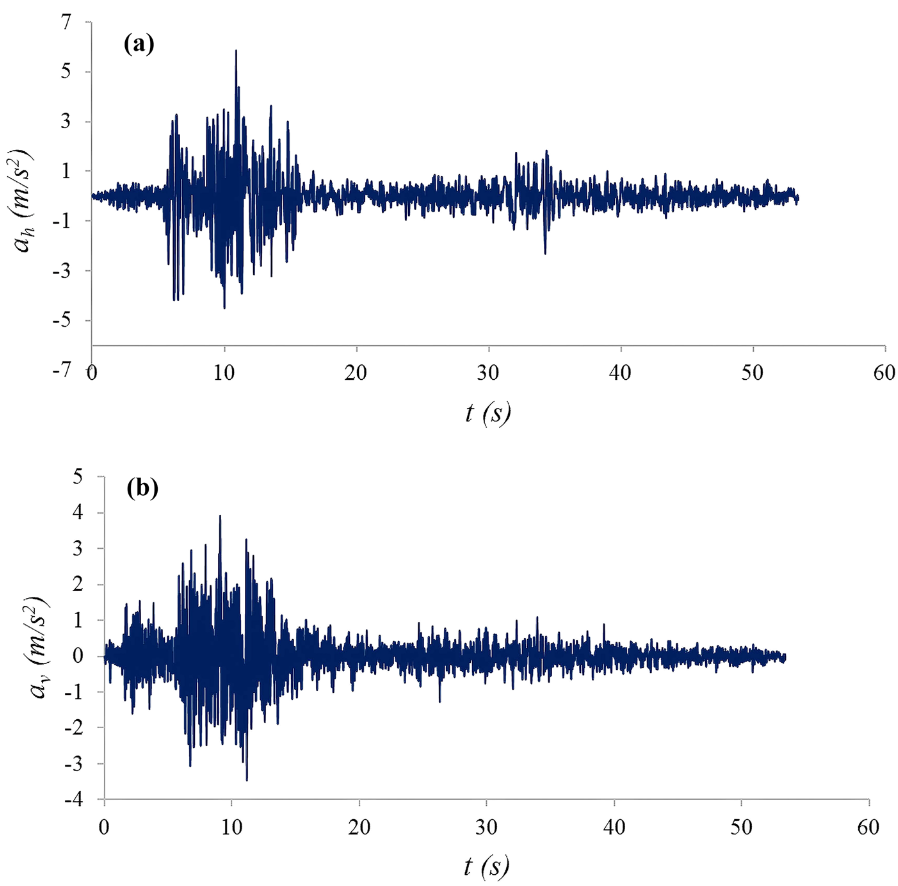

Fig. 8 Manjil earthquake acceleration **a** horizontal component and **b** vertical component

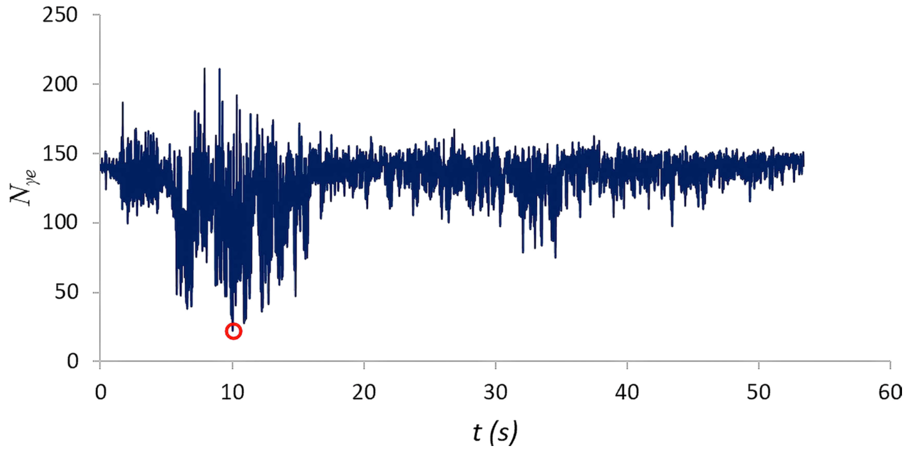

Fig. 9 The time history of $N_{\gamma e}$, obtained by proposed method

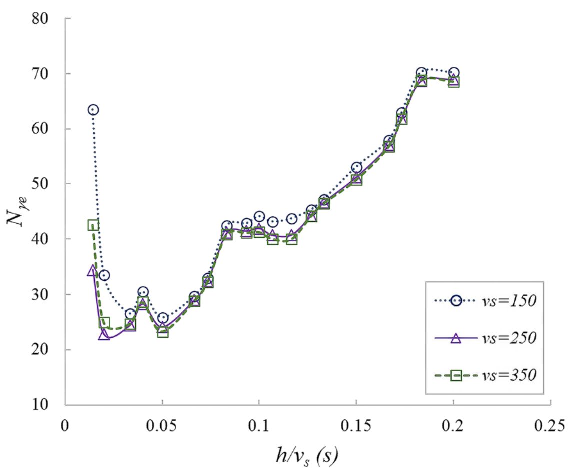

Fig. 10 Effects of V_s on $N_{\gamma e}$ for different h/V_s

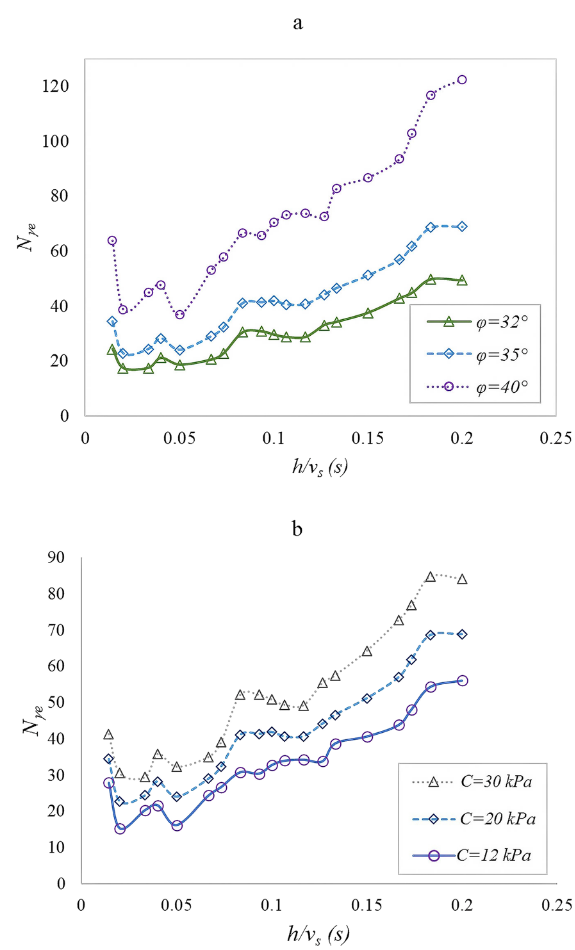

Fig. 11 Effects of the soil shear strength parameters on $N_{\gamma e}$ for different h/V_s **a** effects of the soil frictional angles, **b** effects of the soil cohesion

3.1 Verification of the Proposed Method

To validate the proposed method, the results of two shaking table experiments and previous analytical methods are compared with the proposed method. The first comparison is based on data from a shaking table test conducted by Knappett et al. (2006). Their study involved tests on a strip foundation placed on dry sand with specific parameters such as $\varphi = 36°$, $G_s = 2.65$, $e_{max} = 0.82$, $e_{min} = 0.495$, and a relative density of 67% ($e = 0.6$). Note that G_s, e, e_{max}, and e_{min} represent the specific gravity, void ratio, maximum void ratio, and minimum void ratio, respectively. The footing had a width of 5 cm and was placed on a 30 cm thick soil layer. The vertical stress exerted by the foundation on the supporting soil was approximately 8.42 kPa, slightly below the static bearing capacity of 10 kPa leading to failure triggered by the applied motion. The foundation experienced sinusoidal input motion at a frequency of 3.6 Hz for 3 s. The experimental observations were compared with analytical results proposed by Paolucci et al. (1997). Failure initiation occurred at an acceleration amplitude of 0.16 g, with the failure mechanism becoming evident at accelerations of 0.21 g, 0.26 g, and 0.3 g. It was noted that the failure mechanism changed during each cycle of the seismic acceleration. When the seismic acceleration increased from zero, the center of rotation of the failure surface was at the corner of the foundation. However, when the acceleration decreased from its peak, the center of rotation of the failure surface shifted from the corner of the foundation towards the center due to the moment of the inertial forces.

To apply the proposed method, the shear wave velocity, primary wave velocity, and damping ratio of the soil are approximated at 105 m/s, 196 m/s, and 10%, respectively, as proposed by Seed et al. (1986) considering the level of shear strain effective vertical stress. The results obtained from the proposed method, as presented in Table 1, closely align with the experimental observations across various acceleration amplitudes.

Another experimental study that can be used to validate the proposed method, was conducted by Al-Karni (2001). The experiment involved testing a foundation positioned on dry sand with properties such as $G_s = 2.64$, $e_{max} = 0.95$, $e_{min} = 0.58$, $Dr = 67\%$, and $\varphi = 40°$. The foundation had an embedment depth of $D = 0$ and a width of $B = 1$ m. Two models were tested individually. In the first model, a load of 615 kN was exerted on the soil. In the second model, a load of 205 kN was applied from the foundation to the supporting soil. The input motion was a horizontal acceleration with a frequency of 3 Hz and a linearly increasing magnitude until reaching the critical accelerations that led to failure. The critical accelerations were determined to be 0.08 g for the first model and 0.25 g for the second model. The results are summarized in Table 2. It is worth noting that a shape factor of 0.6 can be utilized when using the equations associated with strip footings to determine the seismic bearing capacity of square footings. A close match is evident between the results obtained using the proposed method (607 and 192 kN) and the values measured in the experiments (615 and 205 kN).

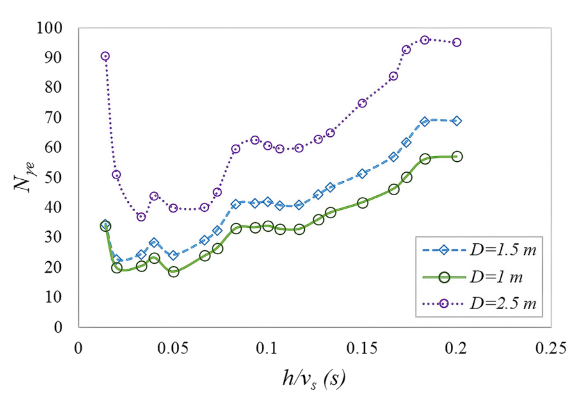

Fig. 12 Effects of the depth embedment on $N_{\gamma e}$ for different h/V_s

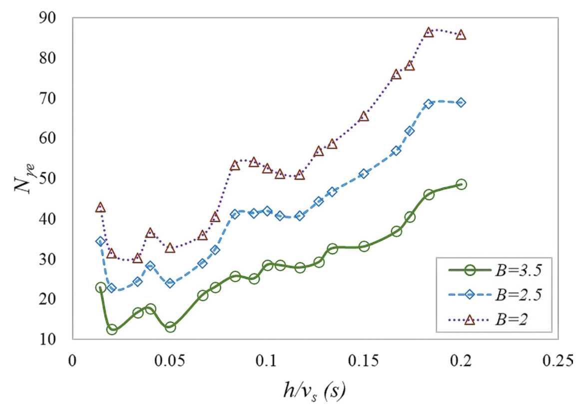

Fig. 13 Effects of foundation width on $N_{\gamma e}$ for different h/V_s

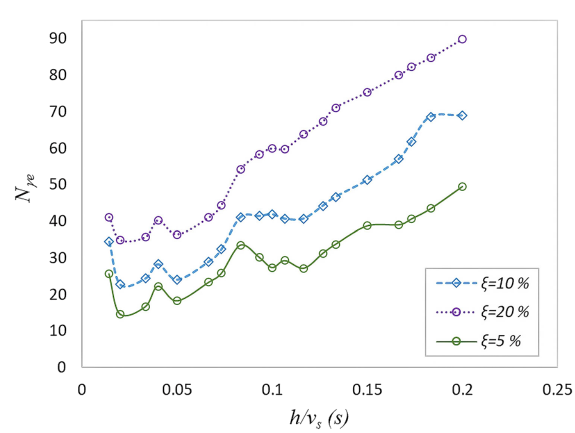

Fig. 14 Effects of damping ratio on $N_{\gamma e}$ for different h/V_s

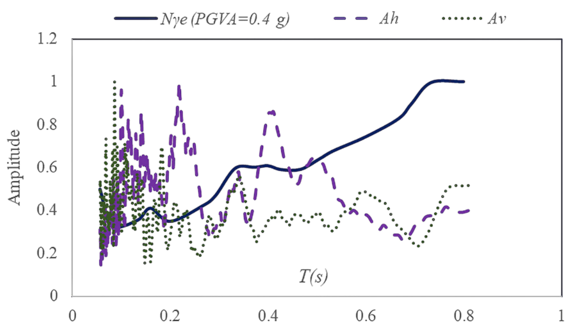

Fig. 15 $N_{\gamma e}$ and smoothed A_h and A_v for different periods

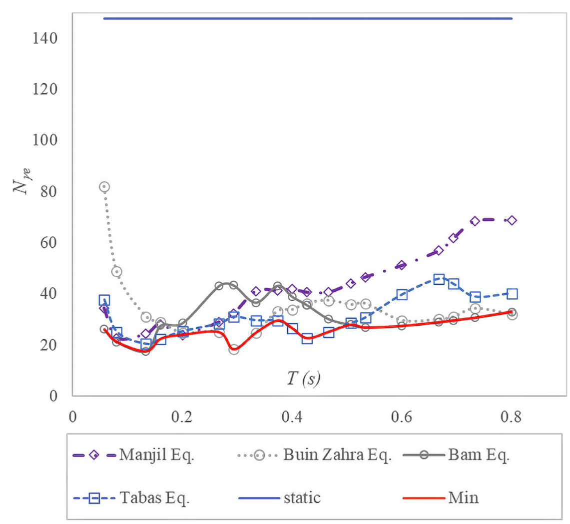

Fig. 16 $N_{\gamma e}$ for different large earthquakes scaled to $PGA = 0.6g$

Figure 7 shows a comparison of the seismic bearing capacity factors obtained by the proposed method with those obtained by available analytical methods, including the characteristic stress method by Kumar et al. (2002), the pseudo-static approach by Choudhury et al. (2005), the upper-bound limit analysis by Soubra (1997 and 1999), the modified pseudo-dynamic method by Pain (2016) and Nadgouda et al. (2021), and the node-based smoothed finite element method by Nguyen et al. (2022). The results were computed for $\varphi = 30°$, $\delta = 0.7\varphi$, $a_{hmax} = 0$, 0.1 g, 0.2 g, and 0.3 g, $a_v = 0$, $\xi = 0.10$, $V_p/V_s = 1.87$, $V_s = 200$ m/s, $B = 2$ m, $h = 5$ m, $w = 6\pi$ *rad/s*, and $D = 0$. The proposed method's results were obtained for both harmonic excitation and the 1990 Manjil earthquake, adjusted to the desired maximum acceleration. The proposed method's results align well with other results when the acceleration is low.

As the acceleration increases, the proposed method's results for harmonic input exhibit slower degradation compared to other analytical solutions. The slight increase in the seismic bearing capacity factor could be attributed to the phase difference of seismic accelerations throughout the depth. In contrast, the proposed method's results for the earthquake input motion depreciate rapidly due to the substantial amplitudes of seismic accelerations across a broad frequency range, triggering significant responses corresponding to the system's natural frequencies. For a 5 m-thick soil layer, at an acceleration magnitude of 0.3 g, the bearing capacity diminishes to zero. However, with a soil layer thickness of 20 m, the seismic bearing capacity coefficient increases to 5.2 due to the alteration in the soil layer's fundamental frequency.

3.2 A Parametric Study on a Large Earthquake

A parametric study was conducted using the 1990 Manjil earthquake with a magnitude of 7.6 as the input motion. Figure 8 shows the seismic accelerations recorded during the earthquake, as reported by the Iran Strong Motion Network database, scaled with peak horizontal and vertical ground accelerations of 0.6 g and 0.4 g, respectively. Soil properties were assumed to be $\varphi_p = 35°$, $\varphi_r = 30°$, $c_p = 20$ kPa, $c_r = 10$ kPa, $V_s = 250$ m/s, $V_p = 1.87\ V_s$, damping ratio of 10%, and unit weight of $\gamma = 17$ kN/m^3. The foundation width and embedment depth were 2.5 m and 1.5 m, respectively. The time history of $N_{\gamma e}$ obtained through the proposed method is shown in Fig. 9, highlighting the minimum value marked by a red circle. The Figure demonstrates that the proposed method can calculate the seismic bearing capacity at any given moment.

The impact of shear wave velocity on $N_{\gamma e}$ was studied by assuming different shear wave velocities while keeping other parameters constant. $N_{\gamma e}$ values were calculated for shear wave velocities of 150, 250, and 350 m/s. Figure 10 illustrates the effect of soil shear wave velocity on $N_{\gamma e}$ for various h/V_s ratios, where T_1 is defined as 4 h/V_s, representing the fundamental natural period of the soil deposit. The curves for different shear wave velocities show a consistent trend, influenced by ground motion characteristics such as frequency content and T_1 or h/V_s. Changes in shear wave velocity or soil deposit thickness affect h/V_s or T_1, leading to fluctuations in $N_{\gamma e}$. Higher T_1 values correspond to either decreases or increases in $N_{\gamma e}$. During intense earthquakes, a reduction in V_s causes $N_{\gamma e}$ to shift towards higher h/V_s values. Critical h/V_s values ranged from 0.02 to 0.05, where seismic bearing capacity reached a minimum due to significant inertial forces effects, indicating a resonance condition. In these conditions, the seismic bearing capacity factor drops substantially to 15% of the static value, emphasizing the necessity of reinforcement techniques such as micropiles beneath the footing. In weaker soil seismic bearing capacity may diminish to zero during a major earthquake.

Shear strength parameters have a significant impact on $N_{\gamma e}$: Fig. 11a shows how the soil friction angle affects $N_{\gamma e}$ for different h/V_s ratios. $N_{\gamma e}$ exhibits a more pronounced fluctuating trend for $\varphi = 40°$ compared to $\varphi = 32°$ and $\varphi = 35°$. The variation of $N_{\gamma e}$ for a soil friction angle of $\varphi = 32°$ follows a similar trend with h/V_s compared to $\varphi = 35°$, but with a smaller amplitude. During a large earthquake, the soil friction angle decreases due to large strains and plastic zones in the soil, leading to a shift in the $N_{\gamma e}$ path to lower levels.

Figure 11b illustrates the impact of soil cohesion on $N_{\gamma e}$ for various h/V_s ratios. $N_{\gamma e}$ increases with higher soil cohesion, with a consistent trend across different cohesion values of 12, 20, and 30 kPa. The minimum of $N_{\gamma e}$ occurs at $h/V_s = 0.05$ and 0.02 for all soil cohesion values. Similarly, during significant earthquakes, a decrease in soil cohesion can cause $N_{\gamma e}$ to decrease following a lower trend.

The impact of embedment depth on $N_{\gamma e}$ for different h/V_s ratios is shown in Fig. 12. Minimum $N_{\gamma e}$ values occur at $h/V_s = 0.05$ and 0.02 for all depths considered. Increasing the embedment depth leads to higher $N_{\gamma e}$ values, therefore, selecting the deepest possible embedment can enhance $N_{\gamma e}$ in seismic regions. For $D = 2.5$ m, the seismic bearing capacity has significantly increased for all h/V_s ratios compared to smaller D values. Furthermore, this figure clearly demonstrates that the depth of embedment is a key factor in seismic stability, and even deep foundations like piles and micropiles exhibit favorable seismic performance.

Figure 13 illustrates the relationship between the foundation width and $N_{\gamma e}$. With an increase in the foundation width (B), $N_{\gamma e}$ decreases, but the overall seismic bearing capacity rises. This increase is due to the seismic bearing capacity formula ($Q_{ue} = 0.5\gamma B N_{\gamma e} \times B$), which is derived by multiplying the $N_{\gamma e}$ factor by B^2. At $h/V_s = 0.05$ the minimum of $N_{\gamma e}$ values and (Q_{ue}) values are 32.9 (1118.6 kN/m), 24 (1275 kN/m), and 13.1 (1364 kN/m) for $B = 2$, 2.5, and 3.5 m, respectively. The rocking moment resulting from structural inertial forces reduces the effective foundation width, leading to a higher trend in $N_{\gamma e}$. However, Q_{ue} decreases due to this reduction in effective width.

The impact of the damping ratio on $N_{\gamma e}$ is depicted in Fig. 14 across various h/V_s ratios. As expected, an increase in the damping ratio leads to a higher $N_{\gamma e}$ value. Additionally, the.

damping ratio mitigates the fluctuation of $N_{\gamma e}$, resulting in a more gradual trend. The curve exhibits a smoother variation with $\xi = 20\%$ compared to $\xi = 10\%$, and $\xi = 5\%$. During a large earthquake, nonlinear soil behavior may elevate soil damping (Seed et al. 1986), causing a slight increase in $N_{\gamma e}$. However, overall $N_{\gamma e}$ values decrease due to a decline in soil shear strength.

Figure 15 illustrates $N_{\gamma e}$ for different fundamental periods of the soil deposit ($T = T_1$) as well as A_h and A_v for Fourier periods (T). The values were normalized with the corresponding maximum value. The average of 15 sequential values was used to smooth the normalized Ah and Av. The minimum value of $N_{\gamma e}$ occurs at a period of $T = 0.2$ ($h/V_s = 0.05$) when the normalized A_h peaks at 1.0 and the normalized value of A_v is equal to 0.32. $N_{\gamma e}$ has a high value at $T = 0.057$ when A_h and A_v have small values. $N_{\gamma e}$ is significantly affected from $T = 0.06$ to $T = 0.5$ s due to the high magnitudes of A_h and A_v for this T range.

Figure 16 illustrates the $N_{\gamma e}$ values for different major earthquakes (reported by the Iran Strong Motion Network database) with the same *PGA* in Iran. The figure clearly shows a significant reduction in bearing capacity for most earthquakes across all T_1 values. The earthquakes in Tabas (1978, $M_w = 7.8$), Bam (2003, $M_w = 6.6$), and Buin Zahra (2002, $M_w = 6.5$) particularly exhibit this pronounced reduction in seismic bearing capacity for almost all T_1 values. On the other hand, the Manjil (1990, $M_w = 7.6$) earthquake demonstrates a similar drastic reduction but with a range of $T_1 = 0.06$–0.3 s. For T_1 values greater than 0.3, a higher seismic bearing capacity is observed. In Fig. 16, the minimum of $N_{\gamma e}$ for all earthquakes is depicted by a red line, showing a range of 78–88% reduction in seismic bearing capacity depending on the fundamental period of the soil deposit. Therefore, due to the substantial decrease in the foundation's bearing capacity during major earthquakes, it becomes necessary to consider the use of deep foundations, such as piles or micropiles, to ensure greater stability, just as the root is necessary to protect the tree from wind.

4 Conclusions

An extended pseudo-dynamic approach was proposed to calculate the seismic bearing capacity for strip foundations on φ-c soils. This approach allows for analysis in the time domain and can directly consider earthquake acceleration records as input excitation. Furthermore, by solving the problem step by step in time, it can account for nonlinear behavior and the reduction of soil resistance and stiffness during large earthquakes. This approach can be combined with numerical methods, limit analysis, and many techniques, in future research to create a more efficient tool for seismic analysis. Additionally, this method can be applied to other seismic geotechnical issues. A limitation of the presented method is that the soil subgrade was considered as a dry viscoelastic medium. Future research could investigate the effects of water saturation. The results of the parametric study for a major earthquake show that the variation of the seismic bearing capacity factor for different ratios of deposit thickness to shear wave velocity follows a distinct trend based on the ground motion's frequency content and the fundamental period of the soil deposit. The study also discusses the effects of foundation width, foundation embedment, and soil damping ratio. Increasing the foundation width leads to a decrease in seismic bearing capacity, but the overall seismic bearing capacity increases. The damping ratio helps mitigate the fluctuation of seismic bearing capacity resulting in a more gradual trend. Increasing the embedment depth leads to higher seismic bearing capacity values. Therefore, selecting the deepest possible embedment can enhance seismic bearing capacity in seismic regions. The significant decrease in the foundation's bearing capacity during major earthquakes highlights the importance of considering the use of deep foundations like piles or micropiles for enhanced stability and safety.

Author Contributions All authors contributed to the study conception and design. Material preparation, data collection and analysis were performed by All authors. The first draft of the manuscript was written by all authors. All authors read and approved the final manuscript.

Funding The authors declare that no funds, grants, or other support were received during the preparation of this manuscript.

Data Availability The datasets generated during and/or analysed during the current study are available from the corresponding author upon a request.

Declarations

Conflict of interests The authors have no relevant financial or non-financial interests to disclose.

References

Akhavan Tavakoli M, Fathipour H, Payan M, Jamshidi Chenari R, Ahmadi H (2023) Seismic bearing capacity of shallow foundations subjected to inclined and eccentric loading using modified pseudo-dynamic method. Transport Geotech 40:100979. https://doi.org/10.1016/j.trgeo.2023.100979

Al-Karni AA, Budhu M (2001) An experimental study of seismic bearing capacity of shallow footings. 4th international conferences on recent advances in geotechnical earthquake engineering and soil dynamics. San Diego, California, p 26–31

Bellezza I (2014) A new pseudo-dynamic approach for seismic active soil thrust. Geotech Geol Eng 32(2):561–576. https://doi.org/10.1007/s10706-014-9734-y

Bellezza I (2015) Seismic active earth pressure on walls using a new pseudo-dynamic approach. Geotech Geol Eng 33(4):795–812. https://doi.org/10.1007/s10706-015-9860-1

Budhu M, Al-Karni A (1993) Seismic bearing capacity of soils. Géotechnique 43(1):181–187. https://doi.org/10.1680/geot.1993.43.1.181

Casablanca O, Biondi G, Cascone E (2023) Bearing capacity of shallow foundations accounting for seismic excess pore pressures. Soil Dyn Earthq Eng 173:108090. https://doi.org/10.1016/j.soildyn.2023.108090

Cascone E, Casablanca O (2016) Static and seismic bearing capacity of shallow strip footings. Soil Dyn Earthq Eng 84:204–223. https://doi.org/10.1016/j.soildyn.2016.02.010

Chen BH, Luo WJ, Xu XY, Hu RQ, Yang XL (2022) Seismic bearing capacity of strip footing with nonlinear mohr-coulomb failure criterion. Int J Geomech 22(10):06022029. https://doi.org/10.1061/(ASCE)GM.1943-5622.0002521

Choudhury D, Nimbalkar S (2005) Seismic passive resistance by pseudo-dynamic method. Géotechnique 55(9):699–702. https://doi.org/10.1680/geot.2005.55.9.699

Choudhury D, Nimbalkar S (2006) Pseudo-dynamic approach of seismic active earth pressure behind retaining wall. Geotech Geol Eng 24(5):1103–1113. https://doi.org/10.1007/s10706-005-1134-x

Choudhury D, Subba Rao KS (2005) Seismic bearing capacity of shallow strip footings. Geotech Geol Eng 23(4):403–418. https://doi.org/10.1007/s10706-004-9519-9

Conti R (2018) Simplified formulas for the seismic bearing capacity of shallow strip foundations. Soil Dyn Earthq Eng 104:64–74. https://doi.org/10.1016/j.soildyn.2017.09.027

Debnath L, Ghosh S (2018) Pseudostatic analysis of shallow strip footing resting on two-layered soil. Int J Geomech 18(3):04017161. https://doi.org/10.1061/(ASCE)GM.1943-5622.0001049

Debnath L, Ghosh S (2021) Modified pseudo-dynamic bearing capacity of strip footing resting on layered soil. Iranian J Sci Tech Trans Civil Eng 45(4):2733–2763. https://doi.org/10.1007/s40996-020-00540-4

Franke KW, Candia G, Mayoral JM, Wood CM, Montgomery J, Hutchinson T, Morales-Velez AC (2019) Observed building damage patterns and foundation performance in Mexico city following the 2017 M7.1 Puebla-Mexico city earthquake. Soil Dyn Earthq Eng 125:105708. https://doi.org/10.1016/j.soildyn.2019.105708

Ganesh R, Kumar J (2022) Seismic bearing capacity of strip foundations with nonlinear power-law yield criterion using the stress characteristics method. J Geotech Geoenviron Eng 148(11):04022083. https://doi.org/10.1061/(ASCE)GT.1943-5606.0002867

Garzón-Roca J, Melentijevic S (2024) Seismic bearing capacity of a footing on sloping frictional soil. Transp Infrastruct Geotechnol. https://doi.org/10.1007/s40515-024-00393-8

Ghosh P (2008) Upper bound solutions of bearing capacity of strip footing by pseudo-dynamic approach. Acta Geotech 3(2):115. https://doi.org/10.1007/s11440-008-0058-z

Ghosh S, Debnath L (2017) Seismic bearing capacity of shallow strip footing with coulomb failure mechanism using limit equilibrium method. Geotech Geol Eng 35(6):2647–2661. https://doi.org/10.1007/s10706-017-0268-y

Hamrouni A, Sbartai B, Dias D (2021) Ultimate dynamic bearing capacity of shallow strip foundations-reliability analysis using the response surface methodology. Soil Dyn Earthq Eng 144:106690. https://doi.org/10.1016/j.soildyn.2021.106690

Iran Strong Motion Network. https://www.bhrc.ac.ir/enismn.

Jiryaei Sharahi M (2022) Extended pseudodynamic method to assess seismic active pressure under seismic loading. Int J Geomech 22(8):04022122. https://doi.org/10.1061/(ASCE)GM.1943-5622.0002451

Jitchaijaroen W, Duong NT, Lai VQ, Sangjinda K, Nguyen TS, Keawsawasvong S, Jamsawang P (2024) Probabilistic analysis of the seismic bearing capacity of strip footings using RAFELA and MARS. Geotech Geol Eng. https://doi.org/10.1007/s10706-024-02857-7

Izadi A, Jamshidi Chenari R, Javankhshdel S, Hemmati Masouleh F (2022) Effect of love wave propagation on the equivalent seismic bearing capacity of shallow foundations using 3D coulomb failure mechanism. Geotech Geol Eng 40(5):2781–2797. https://doi.org/10.1007/s10706-022-02061-5

Izadi A, Nazemi Sabet Soumehsaraei M, Jamshidi Chenari R, Moallemi S, Javankhoshdel S (2021) Spectral bearing capacity analysis of strip footings under pseudo-dynamic excitation. Geomech Geoeng 16(5):359–378. https://doi.org/10.1080/17486025.2019.1670873

Kang X, Zhu J, Liu L (2024) Seismic bearing capacity of strip footings with modified pseudo-dynamic method. KSCE J Civ Eng 28(5):1657–1674. https://doi.org/10.1007/s12205-024-2479-0

Knappett JA, Haigh SK, Madabhushi SPG (2006) Mechanisms of failure for shallow foundations under earthquake loading. Soil Dyn Earthq Eng 26(2):91–102. https://doi.org/10.1016/j.soildyn.2004.11.021

Krishnan K, Chakraborty D (2021) Seismic bearing capacity of strip footing over spatially random soil using modified pseudo-dynamic approach. Comput Geotech 136:104219. https://doi.org/10.1016/j.compgeo.2021.104219

Kumar J, Rao VBKM (2002) Seismic bearing capacity factors for spread foundations. Géotechnique 52(2):79–88. https://doi.org/10.1680/geot.2002.52.2.79

Maleki M, Khezri A, Nosrati M, Mir Mohammad Hosseini SM (2023) Seismic amplification factor and dynamic response of soil-nailed walls. Modeling Earth Syst Environ 9(1):1181–1198. https://doi.org/10.1007/s40808-022-01543-y

Maleki M, Mir Mohammad Hosseini SM (2019) Seismic performance of deep excavations restrained by anchorage system using quasi static approach. J Seismol Earthq Eng 21(2):11–21. https://doi.org/10.48303/JSEE.2019.240810

Maleki M, Nabizadeh A (2021) Seismic performance of deep excavation restrained by guardian truss structures system using quasi-static approach. SN Appl Sci 3(4):417. https://doi.org/10.1007/s42452-021-04415-9

Maleki M, Mir Mohammad Hosseini SM (2022) Assessment of the pseudo-static seismic behavior in the soil nail walls using numerical analysis. Innov Infrastruct Solut 7:262. https://doi.org/10.1007/s41062-022-00861-5

Mortara G (2021) Limit analysis solutions for the bearing capacity of strip foundations under seismic conditions. Géotechnique 73(4):337–352. https://doi.org/10.1680/jgeot.21.00150

Nadgouda K, Choudhury D (2021) Seismic bearing capacity factor Nγe for dry sand beneath strip footing using modified pseudo-dynamic method with composite failure surface. Int J Geotech Eng 15(2):171–180. https://doi.org/10.1080/19386362.2019.1707994

Nadgouda K, Choudhury D (2023) Combined seismic bearing capacity factor using modified pseudo-dynamic approach. Geotech Geol Eng 41:1947–1959. https://doi.org/10.1007/s10706-023-02383-y

Nguyen HC, Vo-Minh T (2022) The use of the node-based smoothed finite element method to estimate static and seismic bearing capacities of shallow strip footings. J Rock Mech Geotech Eng 14(1):180–196. https://doi.org/10.1016/j.jrmge.2021.11.005

Nouzari MA, Jamshidi Chenari R, Payan M, Pishgar F (2021) Pseudo-static seismic bearing capacity of shallow foundations in unsaturated soils employing limit equilibrium method. Geotech Geol Eng 39(2):943–956. https://doi.org/10.1007/s10706-020-01535-8

Pain A, Choudhury D, Bhattacharyya SK (2016) The seismic bearing capacity factor for surface strip footings. Geo-Chicago 2016:197–206. https://doi.org/10.1061/9780784480120.0

Paolucci R, Pecker A (1997) Seismic bearing capacity of shallow strip foundations on dry soils. Soils Found 37(3):95–105. https://doi.org/10.3208/sandf.37.3_95

Rahmani F, Hosseini SM, Khezri A, Maleki M (2022) Effect of grid-form deep soil mixing on the liquefaction-induced foundation settlement, using numerical approach. Arab J Geosci 15(12):1112. https://doi.org/10.1007/s12517-022-10340-x

Saha A, Ghosh S (2015) Pseudo-dynamic analysis for bearing capacity of foundation resting on c-ϕ soil. Int J Geotech Eng 9(4):379–387. https://doi.org/10.1179/1939787914Y.0000000081

Saha A, Ghosh S (2020) Modified Pseudo-dynamic bearing capacity of shallow strip footing considering fully log-spiral passive zone with global center. Iranian J Sci Tech Trans Civil Eng 44(2):683–693. https://doi.org/10.1007/s40996-019-00271-1

Seed HB, Wong Robert T, Idriss IM, Tokimatsu K (1986) Moduli and damping factors for dynamic analyses of cohesionless soils. J Geotech Eng 112(11):1016–1032. https://doi.org/10.1061/(ASCE)0733-9410(1986)112:11(1016)

Soubra A (1997) Seismic bearing capacity of shallow strip footings in seismic conditions. Proc Instit Civil Eng Geotech Eng 125(4):230–241. https://doi.org/10.1680/igeng.1997.29659

Soubra A (1999) Upper-bound solutions for bearing capacity of foundations. J Geotech Geoenviron Eng 125(1):59–68. https://doi.org/10.1061/(ASCE)1090-0241(1999)125:1(59)

Steedman RS, Zeng X (1990) The influence of phase on the calculation of pseudo-static earth pressure on retaining wall. Geotechnique 40(1):103–112. https://doi.org/10.1680/geot.1990.40.1.103

Zhang R, Xiao Y, Zhao M, Jiang J (2020) Seismic bearing capacity of strip footings placed near c-φ soil slopes. Soil Dyn Earthq Eng 136:106221. https://doi.org/10.1016/j.soildyn.2020.106221

Zhong J, Li Y, Yang X (2022) Estimation of the seismic bearing capacity of shallow strip footings based on a pseudodynamic approach. Int J Geomech 22(9):04022143. https://doi.org/10.1061/(ASCE)GM.1943-5622.0002459

Zhou J, Qin C (2023) Limit state analysis of rigid retaining structures against seismically induced passive failure in heterogeneous soils. J Rock Mech Geotech Eng. https://doi.org/10.1016/j.jrmge.2023.04.009